Journal of Applied Fluid Mechanics, Vol. 17, No. 7, pp. 1536-1551, 2024.
Available online at www.jafmonline.net, ISSN 1735-3572, EISSN 1735-3645.
https://doi.org/10.47176/jafm.17.7.2316

Aerodynamic Characteristics of High-speed Train Pantographs Based on Jet Flow Control

S. Huang, B. D. Zhang, Z. W. Li †, J. P. Zhao, W. J. Peng and J. R. Lin

School of Rail Transportation, Wuyi University, Jiangmen, 529020, China

†Corresponding Author Email: lzhw1205@wyu.edu.cn

ABSTRACT

The pantograph is a critical instrument that significantly affects the aerodynamics of high-speed trains, posing a considerable challenge to the energy conservation and environmental protection of trains. This study explores the feasibility and efficiency of a jet-flow control technique in optimising the aerodynamic characteristics of the pantograph. A numerical method was adopted to investigate the effects of various jet-flow parameters, such as the jet positions, velocities and jet-slot widths, on the flow changes around the pantograph and subsequent reduction in aerodynamic drag of the pantograph. The results show that the impact of the jet position is negligible when the jet velocity is lower than the train speed. The aerodynamic drag reduction rate decreased with increasing distance from the pantograph as the jet velocity increased. When the distance between the jet slot and pantograph is less than 0.6 times the height of the pantograph, the aerodynamic drag reduction rate continuously increased with the jet velocity. As the jet slot moved away from the pantograph, the aerodynamic drag reduction rate initially increased rapidly with the jet velocity and then gradually decreased when the velocity surpassed 1.2 times the train speed. In addition, the aerodynamic drag of the pantograph decreased as the width of the jet slot decreased. However, the energy of the whole train can be only saved when the jet velocity is below 0.6 times the train speed. Findings in this study verified the effectiveness of the jet-flow method in reducing the aerodynamic drag of pantographs and provide important engineering guidance for the energy-saving of high-speed trains.

Article History

Received September 21, 2023
Revised January 22, 2024
Accepted February 3, 2024
Available online April 30, 2024

Keywords:

Pantograph
Jet flow control
Aerodynamic drag
Flow velocity
Wake vortex

1. INTRODUCTION

The pantograph, mounted on the roof of an electric train, collects electricity from overhead wires to power the train. It consists of a series of complex framed structures that are completely exposed to air, leading to highly turbulent flow and complex vortex structures. The aerodynamic impact of the pantograph becomes more evident as the train speed increases. Previous research has shown that the aerodynamic drag associated with a pantograph accounts for approximately 8–14% of the overall aerodynamic resistance experienced by a high-speed train (Liu, 2013). The turbulent flow structure of the pantograph must be optimised to minimize its aerodynamic resistance and enhance the current collection.

Over the past few years, the aerodynamic properties of pantographs under various operating conditions have been thoroughly investigated by numerical calculations and model tests. Previous studies have demonstrated that wake vortices significantly affect the fluctuating aerodynamic loads and the aerodynamic noise generated by pantographs (Tan et al., 2018; Kim et al., 2020; Yao et al., 2020; Li et al., 2022). The aerodynamic characteristics of a pantograph is greatly affected by various factors. Lee et al. (2015) conducted wind tunnel tests to examine the effect of the panhead configuration on the wake flow characteristics and aerodynamic drag of a pantograph. They found that a streamlined shape optimised the aerodynamic characteristics compared with a rectangular shape. Wang et al. (2022) also verified that a streamlined shape effectively reduced the aerodynamic drag of a pantograph. Zhang et al. (2017) found that the aerodynamic loads decreased when the pantograph was at the rear position in the knuckle-downstream direction. Sun et al. (2020) proposed that the aerodynamic drag can be significantly reduced by backward shifting of the

NOMENCLATURE

Re	Reynolds number	L_{jet}	distance between the jet slot and the leading edge of the pantograph
H	height of the train	W_{jet}	width of the jet slot
H_p	height of the pantograph	V_{jet}	jet velocity
$y+$	dimensionless thickness of the first layer of the grid	$\overline{V}$	time-averaged velocity
U	free stream velocity (train speed)	$\overline{Vx}$	time-averaged streamwise component of velocity
U_∞	velocity of the incoming flow in the wind tunnel test	C_p	transient pressure coefficient
$\triangle t$	time step	$\overline{C_P}$	time-averaged pressure coefficient
$\triangle l$	grid spacing	C_d	aerodynamic drag coefficient of the train
S	windward cross-sectional area of the scaled train model	F_d	aerodynamic drag of the train
S_B	width of the jet slot	$\triangle F_d$	aerodynamic drag reduction value of the train

pantograph. Xiao et al. (2020) noted that sinking the embedded cavity of the pantograph resulted in a significant reduction in its aerodynamic forces. In addition, the impact of the wind conditions and operational environments on the unsteady flow change and forces of the pantograph have also been investigated (Tang, et al., 2015; Xiu, et al., 2016; Niu, et al., 2017; Li et al., 2018, 2023).

According to Ito (2000) and Satio et al. (2021), the streamlined design is the most effective approach to reduce the pantograph's aerodynamic drag and noise. Yao et al. (2022) optimised the base frame structures and insulator shapes of a pantograph and effectively reduced the aerodynamic drag. Chen et al. (2018) and Yan et al. (2022) found that installing a streamlined faring at the appropriate height effectively decreased the aerodynamic drag and noise of the pantograph. However, the traditional approach of improving the aerodynamic performance through shape optimisation has limitations that make it a challenge to achieve significant progress. Therefore, researchers have begun exploring new methods and technologies to improve train aerodynamics.

Recently, owing to the ongoing research on bionics, researchers attempted to apply bionic surfaces to pantograph designs. Inspired by marine organisms, the optimal pitch and thread diameters of whorl structures based on conches were determined for pantograph rods to reduce drag and noise (Liu & Xu, 2018; Xu et al., 2020). Zhang et al. (2021) discovered that applying spanwise corrugated structures to pantograph rods with the appropriate wavelengths and ripple amplitudes could reduce the aerodynamic sound levels. Active flow control is another promising technique. Mitsumoji et al. (2015) found that installing a plasma actuator on the pantograph panhead managed the flow separation and decreased the turbulence intensity at the rear of the panhead. This finding supports the notion that employing the air suction method can serve as an alternative approach to mitigate the aerodynamic noise caused by the panhead. Similarly, Huang et al. (2021) implemented an air jet in the streamwise direction of a grooved pantograph platform, which significantly reduce the noise by 6.04 dB. Huang et al. (2020) confirmed the effectiveness of optimising the train aerodynamics through the jet flow.

This study employed the improved delayed detached eddy simulation (IDDES) model to investigate the impact of various jet-flow parameters on the transient flow around a pantograph and the reduction in aerodynamic drag. The relationships between the jet-flow velocities, positions, and jet-slot widths and aerodynamic resistance of the pantograph were examined to provide guidance for the application of jet-flow method in reducing the aerodynamic resistance of high-speed trains.

2. METHODOLOGY

2.1 Calculation Model

To enhance the computational efficiency and meet the turbulence model requirements of grid generation, a 1/16-scale train model with three cars was utilised, as shown in Fig. 1(a). The operational speed was selected as 300 km/h. At this speed, the Reynolds number (Re) is approximately 1.30×10^6, surpassing the critical Re of 3.6×10^5. Therefore, the flow field was considered as self-simulated (Dong et al., 2019; Che et al., 2023a).

The train height (H) is approximately 0.23 m (3.7 m for the full-scale train model), while its width and length are approximately 0.92H and 20.65H, respectively. The pantograph, which consists of upper, bottom, and base frames and the panhead was mounted near the end of the middle car. The dimensions of the pantograph are showed in Fig. 1(b), i. e. the length, width, and height of 1.35H, 0.52H, and 0.54H, respectively.

A cuboid domain was created, with a length, width, and height of 116H, 26H, and 22H, respectively. The train model was located at the spanwise centre of the domain, the distance between the train head and the domain entrance was measured as 22H, whereas the rear was approximately 73H from the domain exit, as shown in Fig. 2. Constant velocity inlet was assigned to the domain entrance, with a specific velocity corresponding to the train speed. A zero-pressure outlet boundary condition was assigned to the domain exit, and the upper and side surfaces were subjected to symmetry plane conditions. To simulate the relative motion between the

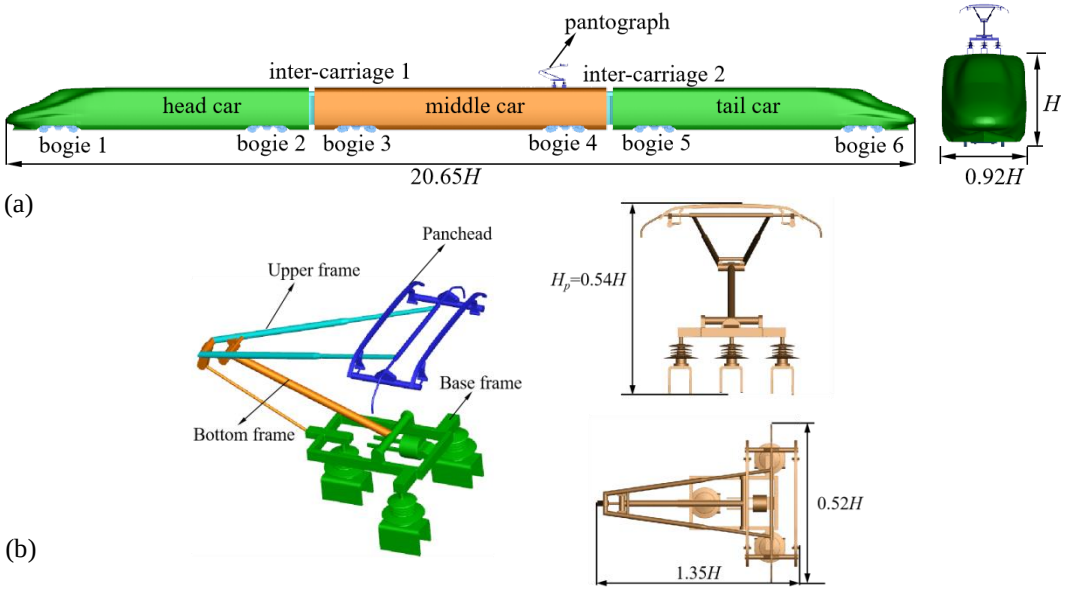

Fig. 1 Geometry and dimensions of the model: (a) the whole train and (b) pantograph

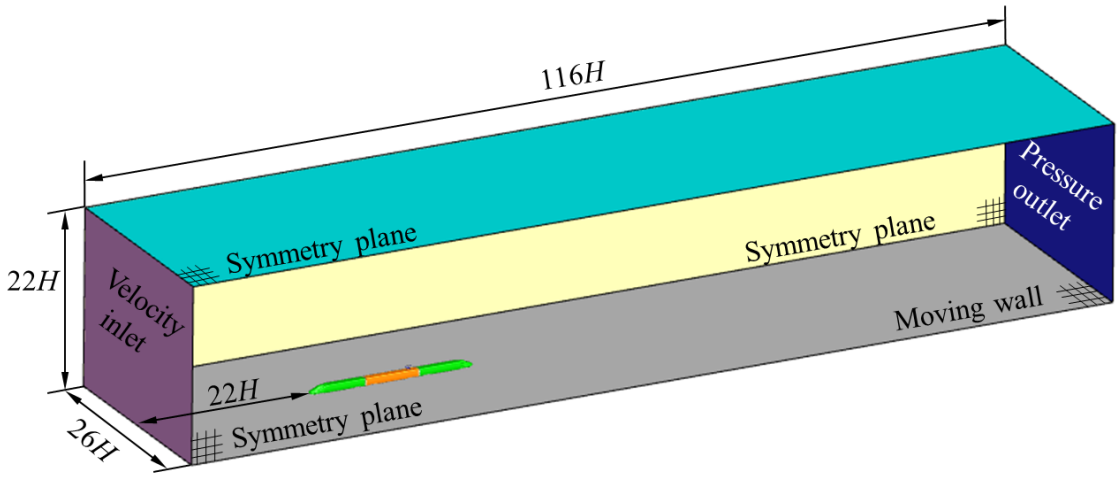

Fig. 2 Domain establishment and boundary condition settings

train and the ground, a moving wall with velocity equal to the train speed was applied to the lower surface (Huang et al., 2016).

The trimmed mesh technology implemented in the Star CCM+ software was utilised for improved numerical accuracy and convergence (Xia et al., 2017; Meng et al., 2021). To achieve mesh-independent results, three sets of grids were established: coarse, medium, and fine meshes, all of which were built with varying grid sizes using the same strategy. The total number of meshes for each set were 17, 34, and 68 million, respectively. The average value of $y+$ was calculated as approximately 1.2, which satisfies the boundary layer solution requirement of the turbulent model.

Taking the medium mesh as an example, the surface grids for the car body and pantograph, which were surrounded by 10 prism grids with an overall thickness of 3 mm and growth rate of 1.2 were demonstrated in Fig. 3(b). Four mesh-refined regions were built in this study, as shown in Fig. 3(c). Refined region 1 encompassed the entire train model, with a length, width, and height of 43H, 2.2H, and 3H, respectively. The wake region was significantly longer than the upstream region to ensure the precise simulation of the wake flow. Because the flow change mainly occurred near the train's surface, a refined region 2 was created closer to the train, with a length, width, and height of 23H, 1.6H, and 2H, respectively. The other two refined regions, 3 and 4, were established around the pantograph. The length, width, and height of refined region 4 were 7H_p, 1.3H_p, and 1.25H_p, respectively. The length of refined region 3 was extended to 12H_p to simulate the wake flow of the pantograph.

Figure 4(b) shows the comparison between the time-averaged flow velocities of the different meshes along line 1, located in the wake region of the pantograph panhead. The specific location of line 1 is shown in Fig. 4 (a).

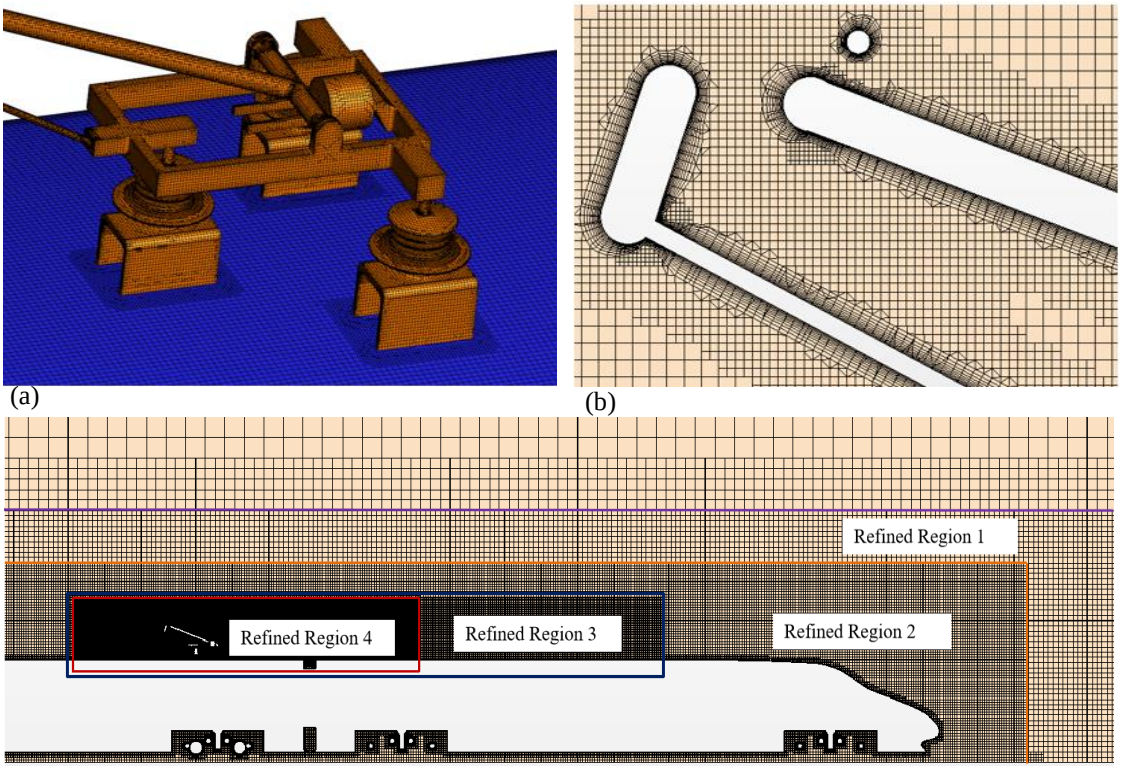

Fig. 3 Computational grid: (a) surface grid, (b) boundary layer around the pantograph, and (c) refined regions

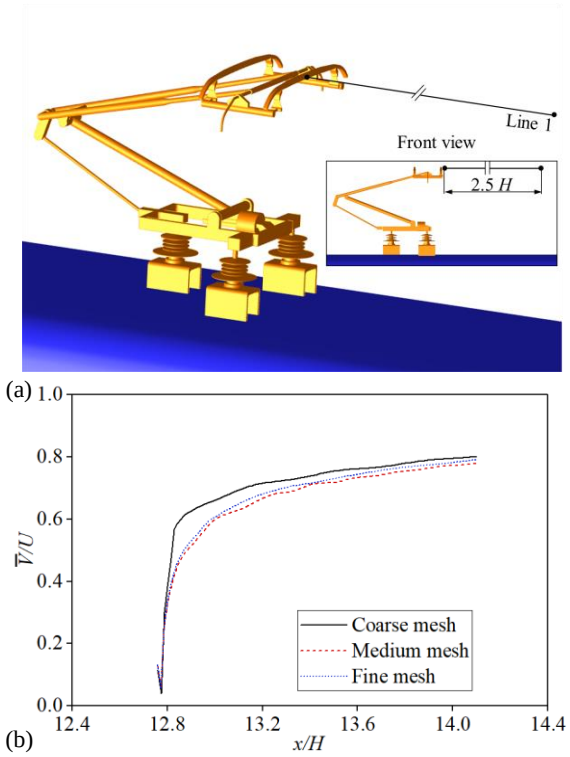

Fig. 4 Comparison between various meshes: (a) position of the line and (b) flow velocity along the line

According to Fig. 4(b), the velocity along line 1 exhibited significant fluctuations within the near-wake area of the panhead when comparing the medium and coarse meshes, with the maximum difference reaching 26%. The results of the fine mesh fit well with those of the medium mesh, with a maximum difference of 3%. This indicates that no significant changes occurred as the computational grid increased, and that the mesh satisfied the independence requirement. Therefore, the medium mesh was selected for the calculations.

2.2 Turbulence Model and Solution Schemes

Numerical calculations were performed using ANSYS Fluent software (Ansys, 2019). The transient IDDES turbulence model based on *SST k–ω* has demonstrated its efficacy in investigating the aerodynamics of trains (Niu et al., 2018; Wang et al., 2019; Niu et al., 2020; Tan et al., 2020). The length scale of the IDDES model can be expressed as

$$l_{IDDES} = \tilde{f}_d(1 + f_e)l_{SST} + (1 - \tilde{f}_d)l_{LES} \quad (1)$$

$$\tilde{f}_d = max\{(1 - f_d), f_B\} \quad (2)$$

$$f_e = max\{(f_{e1} - 1), 0\}\psi f_{e2} \quad (3)$$

In Eq. (2),

$$f_d = 1 - \tanh\,(8r_d)^3 \quad (4)$$

$$f_B = min\{2\exp(-9\alpha^2), 1.0\} \quad (5)$$

$$\alpha = 0.25 - \mathrm{d_w}/\mathrm{h_{max}} \quad (6)$$

where r_d is borrowed from the SA model as reported by (Shur et al., 2008); d_w represents the distance to the wall, and $\mathrm{h_{max}} = \max\{\mathrm{h_x}, \mathrm{h_y}, \mathrm{h_z}\}$ represents the maximum local grid spacing.

In Eq. (3),

$$f_{e1}(d_w/h_{max}) = \begin{cases} 2\exp(-11.09\alpha^2) & if\ \alpha \geq 0 \\ 2\exp(-9.0\alpha^2) & if\ \alpha < 0 \end{cases} \quad (7)$$

$$f_{e2} = 1.0 - \max\{f_t, f_l\} \quad (8)$$

$$f_t = tanh[(c_t{}^2 r_{dt})^3] \quad (9)$$

$$f_l = tanh[(c_l{}^2 r_{dl})^{10}] \quad (10)$$

where r_{dt} and r_{dl} are the turbulent and laminar analogues of r_d, respectively. c_t and c_l are the model constants that are dependent on the RANS model and should be readjusted to ensure that f_{e2} is zero, when either r_{dt} or r_{dl} is close to 1.0.

Based on the above equations, it can be concluded that when $r_{dt} \ll 1$, $\tilde{f}_d = f_B$, and the calculation automatically switches to LES mode. Otherwise, the DES mode is activated.

An initial steady-state calculation of 20000 steps was conducted to establish a fully developed flow field and achieve a converged solution. Then, a second-order implicit transient calculation was activated using SIMPLE algorithm to handle the pressure–velocity coupling (Wang et al., 2020). The convective term of momentum was discretised using a bounded central differencing scheme (ANSYS, 2022) for spatial discretisation, while the turbulent kinetic energy and dissipation rate terms were discretised using a second-order upwind scheme. The residuals were all set as 10^{-6} to achieve higher solution convergence. According to the CFL conditions, the time step Δt used for the three sets of meshes was determined as 1.5×10^{-4}, 8×10^{-5}, and 4×10^{-5}, respectively. The transient calculation time was 0.6s to ensure the full development of the turbulent flow and to collect the unsteady aerodynamic data. Then, an additional 0.4s was calculated with the data sampling option to obtain time-averaged aerodynamic statistics. The total transient calculation time ensures that the air flow passes approximately 3.6 times the entire domain and 20 times the total length of the train model, and the time averaging time makes the flow pass through 8 times the train length. Additionally, as showed in Fig. 5, the aerodynamic drag data of the pantograph within the averaging time changes periodically with stable average value, which ensures the effectiveness of the averaging time.

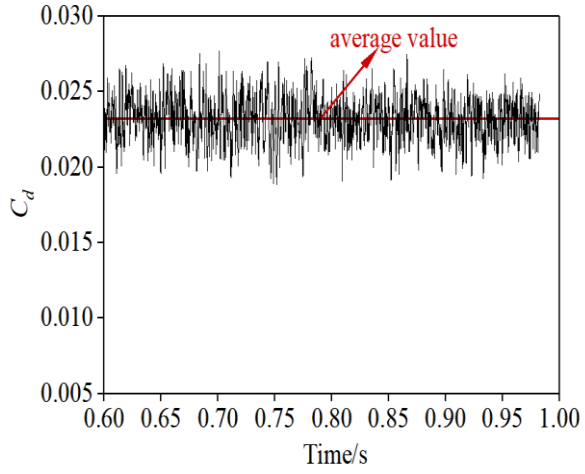

Fig. 5 Aerodynamic drag coefficient of the pantograph within the averaging time

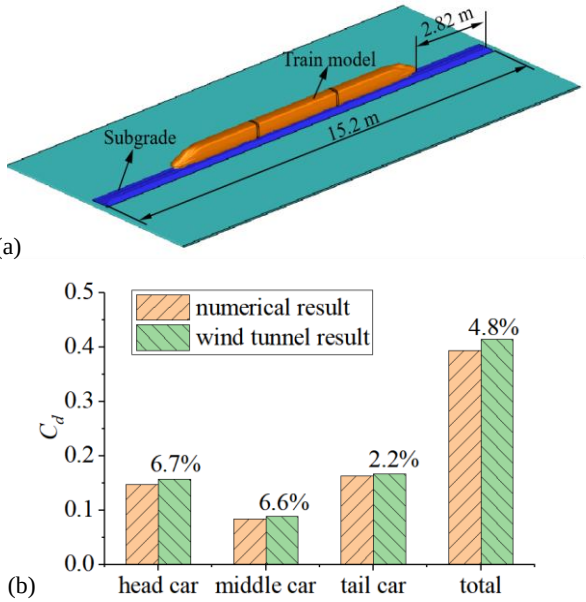

Fig. 6 Results comparison between simulation and test: (a) wind tunnel models and (b) comparison of the aerodynamic drag coefficient

2.3 Algorithm Verification

In order to validate the accuracy of the numerical algorithm, the drag coefficient of the train was compared with the results of a wind tunnel test conducted by Zhang et al. (2018). The wind tunnel test utilised a 1/8-scale train model and a ballast subgrade of 15.2 m in length on the floor, as shown in Fig. 6(a). The calculation model was created based on the wind tunnel model, and the same grid strategy and solvers were adopted. The aerodynamic drag coefficient C_d, calculated by Eq. (11) for each car was compared, as shown in Fig. 6(b). The discrepancy between the results was less than 7%, proving that the computational accuracy of the numerical approach meets the requirements of engineering research.

$$C_d = \frac{F_d}{0.5\rho U_\infty{}^2 S} \quad (11)$$

where F_d represents the aerodynamic drag; U_∞ is the incoming flow velocity, and 60m/s was selected in the wind tunnel test; S is the windward cross-sectional area, which is 0.175m^2 for the scaled train model.

3. RESULTS AND DISCUSSION

3.1 Aerodynamic Drag and Flow Structure of Pantograph Without Air Jet

Pantographs are typically attached to the top of trains and are exposed to the surrounding atmosphere. Based on the quantitative data, pressure drag dominated the total aerodynamic resistance. The interaction between the streamwise and wake flows produces variances in the pressure on the pantograph surface, particularly on the bottom frame and panhead components (Tan et al., 2018; Kim et al., 2020). These components had bluff geometries

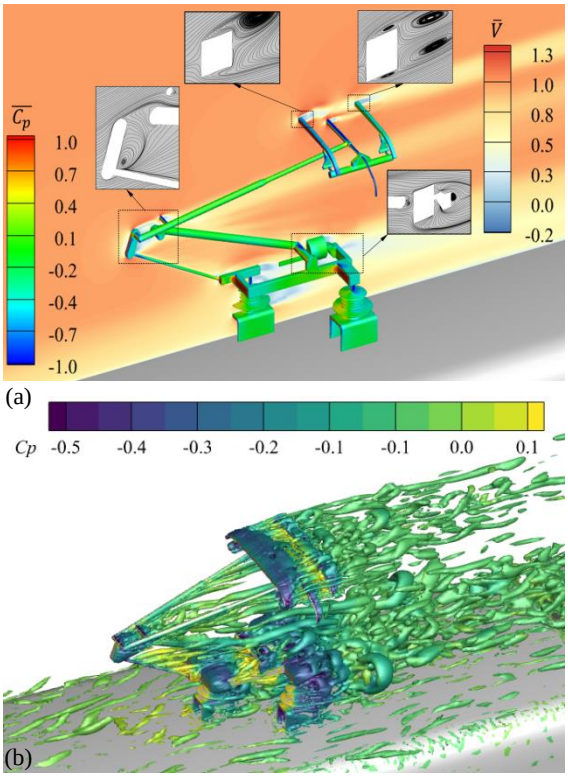

Fig. 7 Flow structures around the pantograph: (a) surface pressure and velocity in vertical plane Y = 0 and (b) iso-surface of Q (Q = 5.5 × 10^6)

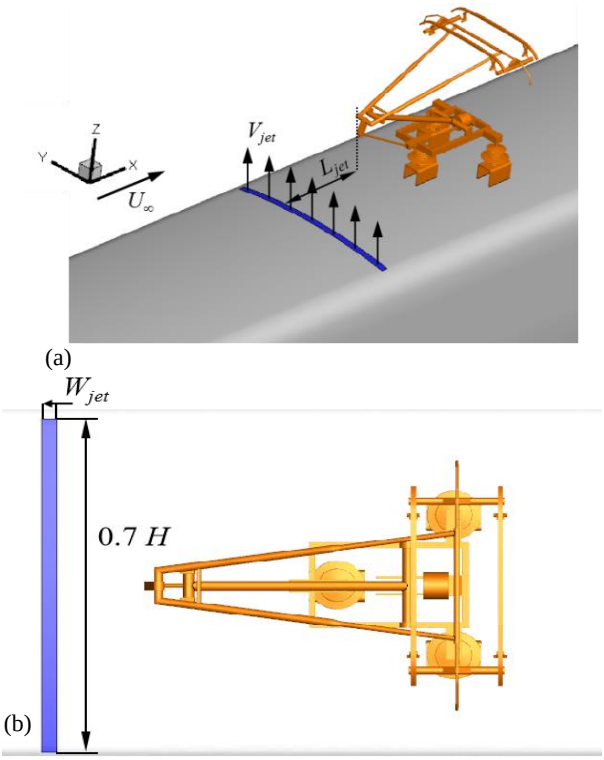

Fig. 8 Schemes of the air-slot jet: (a) axial view and (b) top view

on both the windward and leeward sides, contributing to 57% and 34% of the overall aerodynamic resistance of the pantograph, respectively.

The underlying mechanism responsible for the aerodynamic drag experienced by the pantograph was investigated, including the analysis of pressure distributions on individual parts and the assessment of the surrounding flow structures. Figure 7(a) shows the velocity field along the central longitudinal plane and local streamlines around some important components of the pantograph, and the pressure contours on the pantograph surface. Because the upstream air flowed towards the front surface of the pantograph, a large positive pressure was generated. Subsequently, the accelerated flow separated from the surface of each component, giving rise to a sequence of vortices that predominantly gathered at the rear of the panhead and base frame, as shown in Fig. 7(b). This led to a substantial negative pressure on the leeward surface.

3.2 Effect of Jet Velocity on the Aerodynamics of Pantograph

The primary objective of this study is to set an air-slot jet in front of the pantograph to form an air curtain that minimises the impact of the airflow passing through the pantograph. The jet slot was placed at a specific distance (L_{jet}) away from the leading edge of the pantograph. The width was set to W_{jet} and the length was fixed at 0.7H. It covers the entire top surface with its two ends extending to the edge of the chamfer, as indicated in Fig. 8.

The aerodynamic drag reduction rate, η, is defined and calculated by the following formula.

$$\eta = \frac{C_{d-original} - C_{d-jet}}{C_{d-original}} \times 100\% \quad (12)$$

where $C_{d-original}$ and $C_{d\text{-}jet}$ represent the aerodynamic drag coefficient of the pantograph with and without an air jet, respectively. When the value of η is positive, the pantograph's aerodynamic drag can be mitigated using the air-slot jet method; otherwise, the drag increases.

Figure 9(a) shows the correlation between the pantograph's aerodynamic drag reduction rate and jet velocities at various positions. When the jet slot was close to the pantograph (L_{jet}/H_p < 0.6), the reduction in aerodynamic drag increased as the jet velocity increased. However, as the jet slot gradually moved away from the pantograph, the aerodynamic drag reduction rate initially underwent a rapid increase with the jet velocity, followed by a gradual decrease when the jet velocity surpassed 1.2U. At this point, the drag reduction effect was relatively stable without any discernible fluctuations.

Figure 9(b) and (c) demonstrate the changes in the aerodynamic drag reduction rate of individual components with the jet velocity when the jet slot was located at distances of 0.2H_p and 1.0H_p from the pantograph. Notably, the jet slot significantly affected the aerodynamic drag experienced by the base and bottom frame sections, whereas its effect on the two upper sections was minimal. As the jet slot approached the pantograph, the aerodynamic drag of the base frame decreased as the jet velocity increased. In contrast, the aerodynamic drag of the bottom frame increased. As the jet slot moved away from the pantograph, the aerodynamic

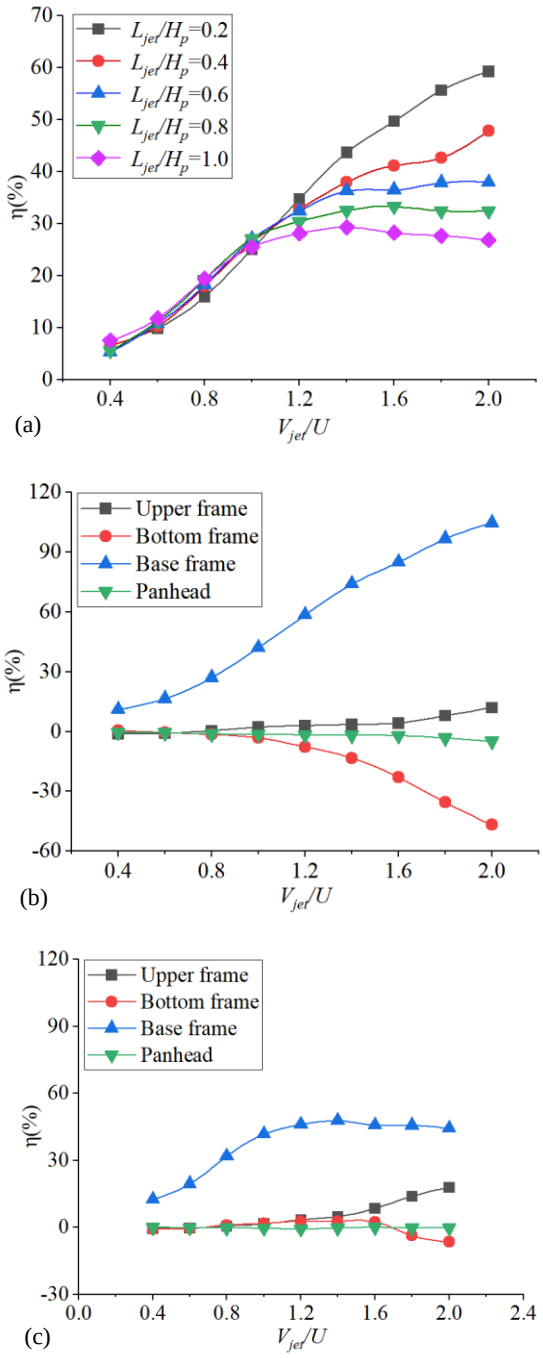

Fig. 9 Correlation between η and V_{jet}: (a) the whole pantograph at different jet positions, (b) each component of the pantograph at jet position L_{jet}/H_p = 0.2, and (c) each component of the pantograph at jet position L_{jet}/H_p = 1.0

resistance of the base frame exhibited an initial rapid increase with the jet velocity, followed by a gradual change when the jet velocity surpassed 1.2*U*. The aerodynamic resistance of the bottom frame initially decreased and then increased when the jet velocity exceeded 1.6*U*. The aerodynamic resistance of the upper frame and panhead slightly changed with the jet velocity. The aerodynamic drag of the base frame had the greatest contribution to the total aerodynamic resistance of pantograph, while the contribution of the bottom frame was minimal, accounting for only 1% of the total. Therefore, the overall aerodynamic resistance of the pantograph followed a trend similar to that of the base frame.

The streamwise component of the time-averaged velocity ($\overline{Vx}$) distributed in a central vertical plane under different jet velocities at positions L_{jet}/H_p =0.2 and L_{jet}/H_p =1.0, are shown in Fig. 10. To demonstrate the airflow changes in front of each component of the pantograph, space lines were set in front of each component, as shown in Fig. 11. The velocities along each space line are compared in Fig. 12.

It can be seen in Fig. 10(a) and 12(a) that when the jet flow was positioned near the front edge of the pantograph, the vertical jet flow interrupted the streamwise flow in the boundary layer, resulting in air stagnation at both the front and rear of the jet slot, accompanied by the generation of vortices on both sides. This phenomenon reduced the speed of air flowing towards the base frame. When the jet velocity was low, the backward vortex appeared flat, with its core close to the roof of the middle car, denoted as *V1*. This was attributed to the dominance of the far-field flow and the small angle of the synthetic velocity. As the jet velocity increased, both the magnitude and angle of the synthetic velocity increased. The airflow at the bottom of the base frame was sucked and rolled up rapidly by the jet flow, causing the backward vortex to increase and the core to move upward, denoted as *V2* and *V3*, respectively. In addition, as the jet velocity increased, the air velocity in front of the base frame flowed in the reverse direction with increasing values under the impact of vortices, which exerted a gradual negative pressure on the windward side of the base frame, as demonstrated in Fig. 13(a). Consequently, the aerodynamic resistance of the base frame continuously decreased with the jet velocity.

The aerodynamic resistance of the bottom frame continuously increased with the jet velocity. This was attributed to the speed-increasing synthetic air that flowed directly towards its front, exerting a significant positive pressure on its windward surface. Conversely, the airflow in front of the upper frame and panhead was minimally affected by the jet flow. Furthermore, the relatively small size of the framed structure resulted in minimal changes in the aerodynamic resistance of the panhead and upper frame compared with the other two frames. Therefore, the pantograph exhibits a comparable upward trend as that of the base frame in terms of the aerodynamic drag reduction, which can be attributed to the changes in the aerodynamic drag experienced by the base frame compared with the bottom frame.

As the jet slot moved away from the pantograph, the impact of the vertical jet flow on the pantograph weakened. As shown in Fig. 10(b) and 12(b), similar to the case in which the jet slot is close to the pantograph, the jet flow reduced the air in front of the base frame. However, the energy was insufficient to absorb the air to reverse the air's movement. Thus, the velocity in front of the base frame persisted in the streamwise direction. According to the findings in Fig. 13(b), the flow velocity initially decreased with the jet velocity owing to the blocking effect, which decreased the positive pressure

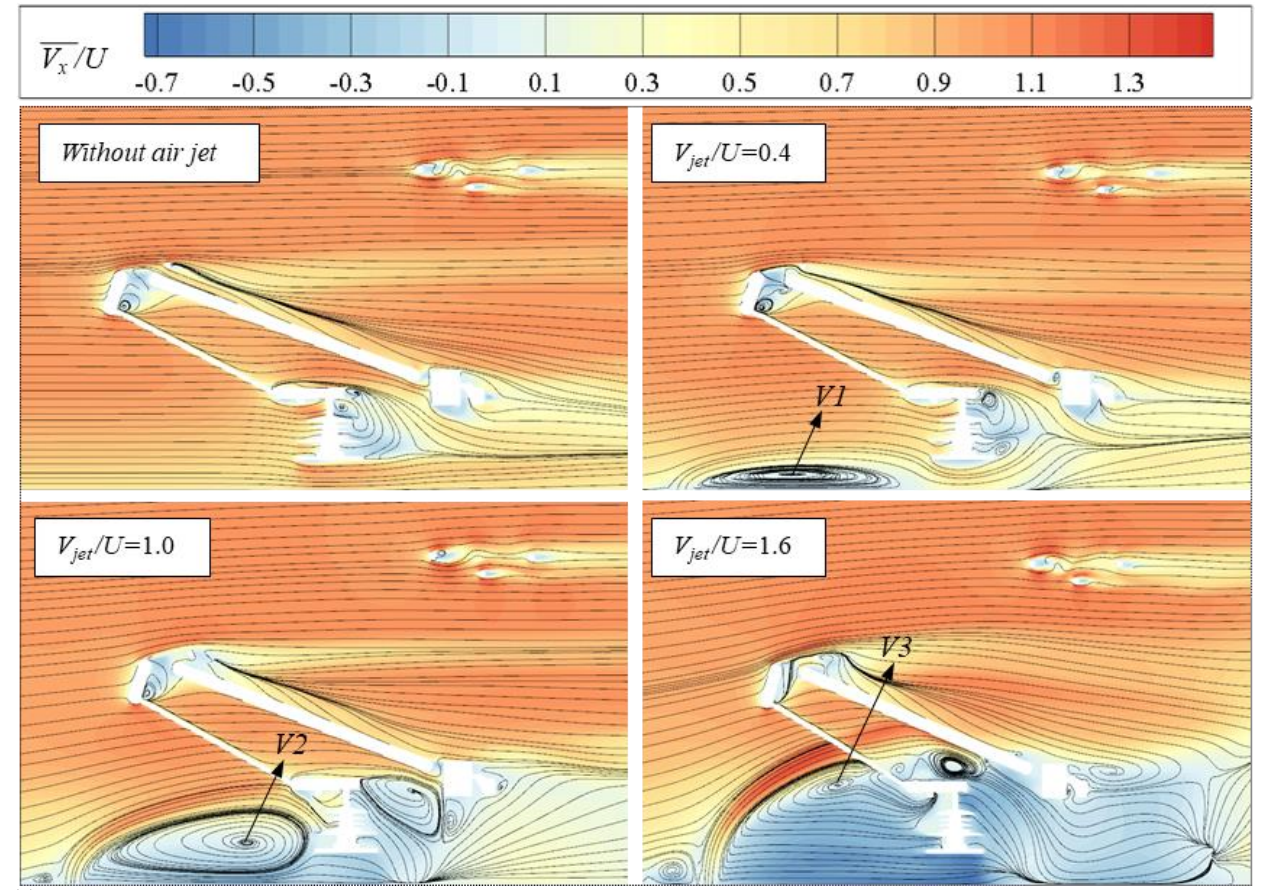

(a)

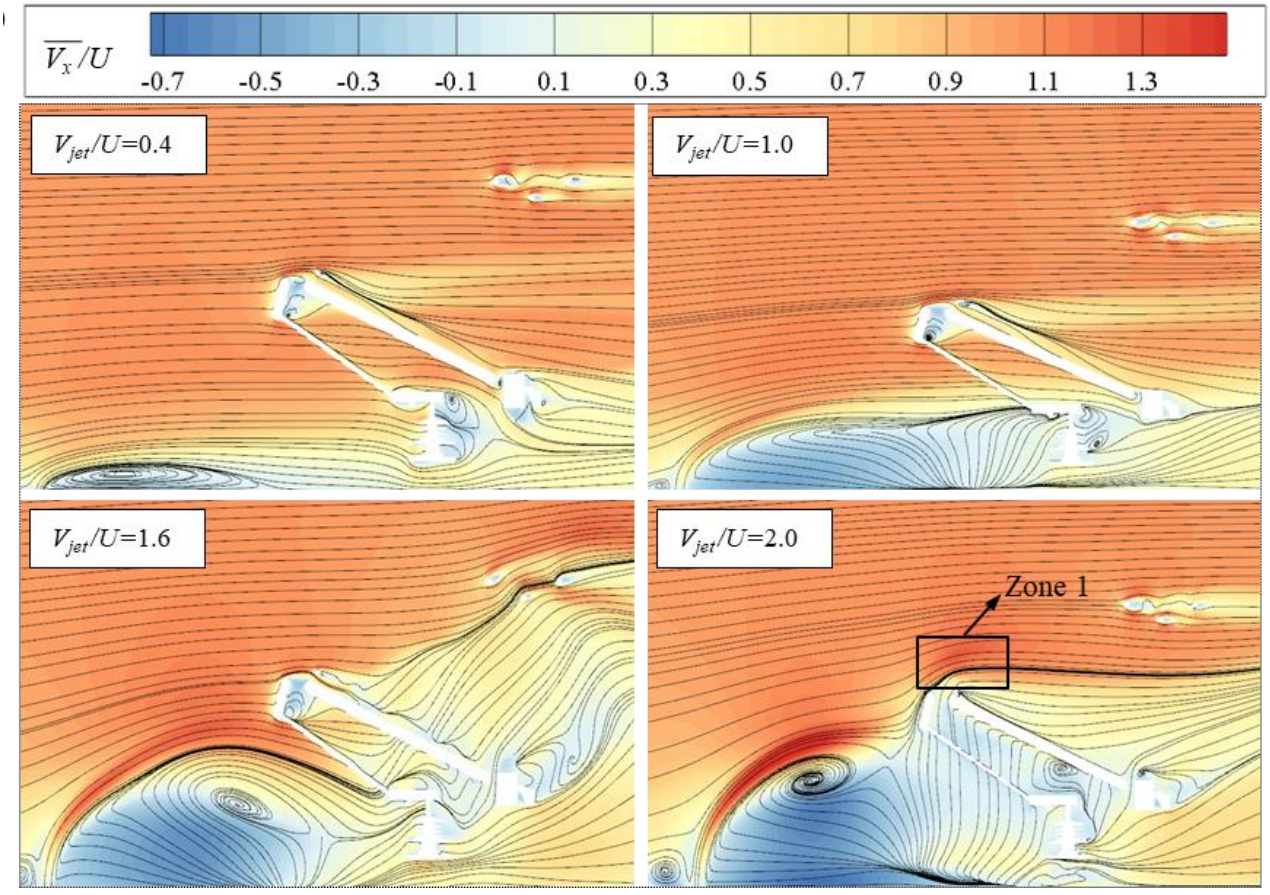

(b)

Fig. 10 Flow velocity change with jet velocity in a vertical plane *Y = 0* at different positions: (a) L_{jet}/H_p = 0.2 and (b) L_{jet}/H_p = 1.0

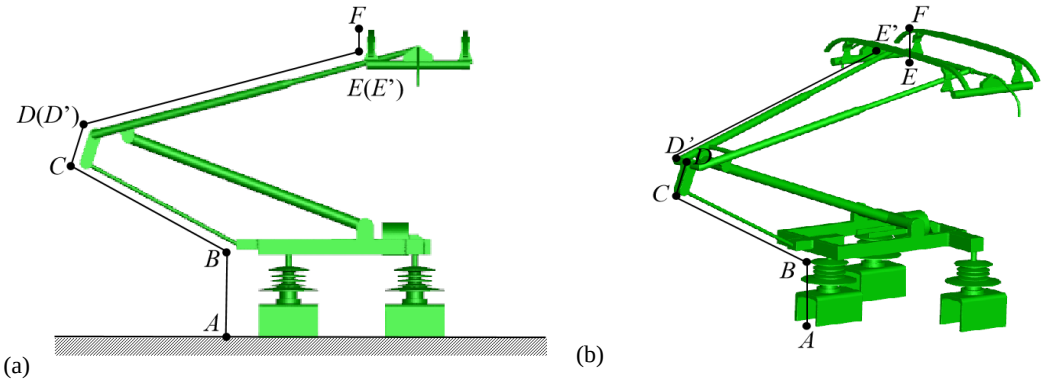

(a) (b)

Fig. 11 Setting of space lines in front of each component of the pantograph: (a) front view and (b) axis view

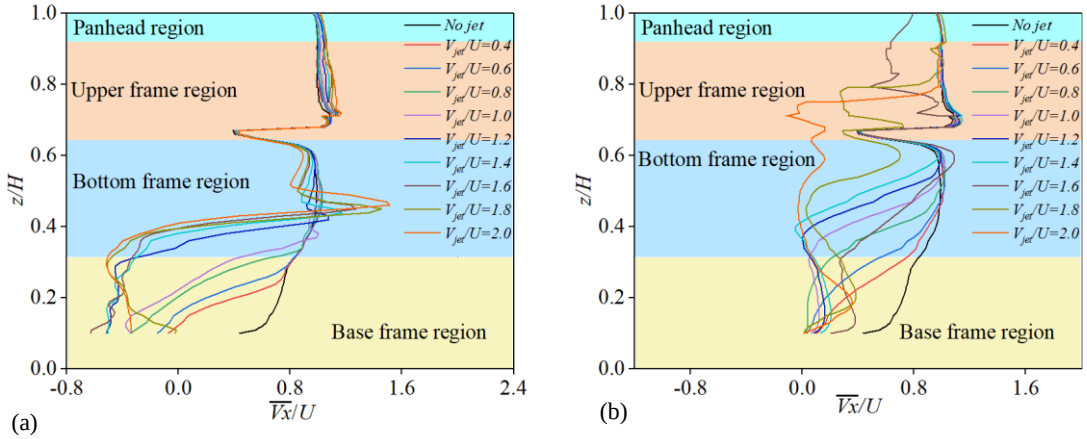

(a) (b)

Fig. 12 $\overline{Vx}$ distributions along various spatial lines in front of the pantograph: (a) jet slot at L_{jet}/H_p= 0.2 and (b) jet slot at L_{jet}/H_p = 1.0

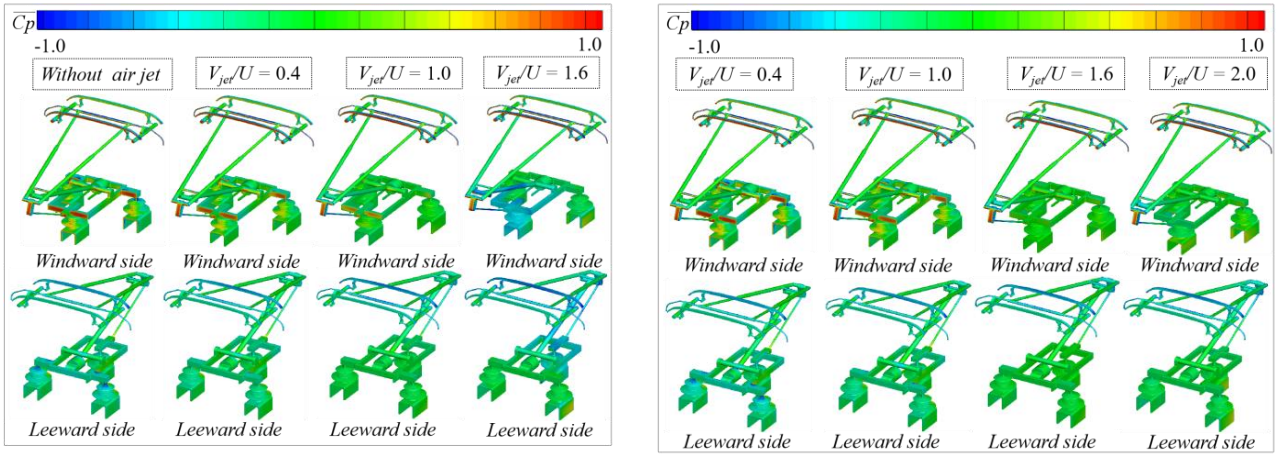

(a) (b)

Fig. 13 Pressure change with jet velocities at different positions: (a) L_{jet}/H_p = 0.2 and (b) L_{jet}/H_p = 1.0

exerted on the windward surface of the base frame. Therefore, the aerodynamic resistance of the base frame decreased with the jet velocity. As the jet velocity progressively increased, the composite angle of the upstream and jet flows increased, thereby causing the primary far-field flow to move upward prematurely and vigorously. However, the energy of the synthetic flow remained insufficient to completely disengage from the influence of the main far-field flow. Consequently, the synthetic flow moved downward when it flowed near the pantograph, leading to an increase in the streamwise air velocity in front of the base frame and a subsequent increase in the positive pressure at the front surface of the base frame. This phenomenon accounts for the decreasing rate of aerodynamic drag reduction in the base frame at higher jet velocities. In addition, the expanding

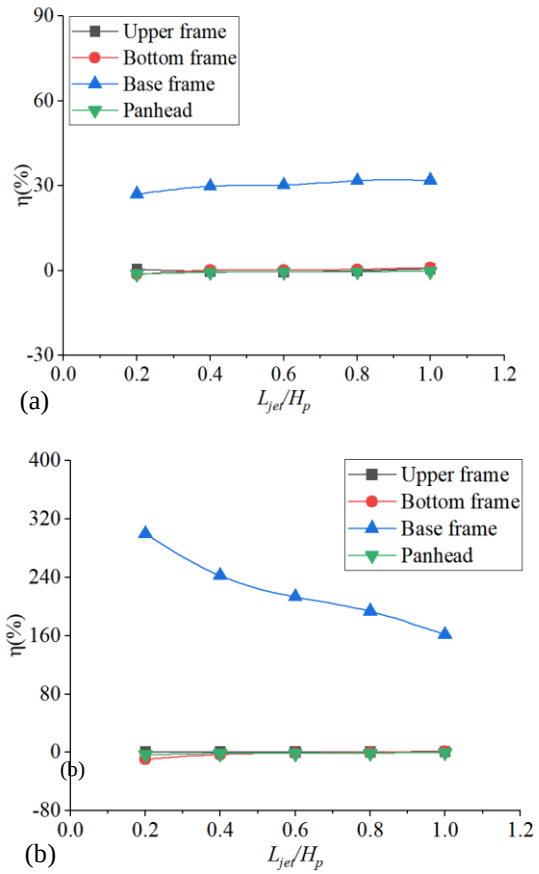

Fig. 14 Correlation between η and L_{jet}: (a) at jet velocity V_{jet}/U = 0.8 and (b) at jet velocity V_{jet}/U = 1.6

speed-decreasing area in front of the pantograph contributed to a slight reduction in the aerodynamic resistance of the bottom frame as the jet velocity increased. However, when the jet velocity reached 1.6*U*, the rapid downward synthetic flow induced a rapid increase in the air velocity in front of the bottom frame. As a result, the aerodynamic resistance of the bottom frame rapidly increased. It should be noted that the airflow in front of the upper frame and panhead was primarily influenced by the main far-field flow rather than the jet velocity at a low level. Nonetheless, as the jet velocity increased, particularly at 1.6*U* and beyond, the jet flow propelled the main flow upwards and traversed over the frontal edge of the upper frame with accelerating velocity, as shown in zone 1 in Fig. 10(b). This leads to a significant negative pressure at the leading edge of the upper frame. At higher jet velocities, the aerodynamic drag of the upper frame decreased as the upward flow decreased the streamwise component velocity in front of the rods.

3.3 Effect of Jet-Slot Positions on the Aerodynamics of Pantograph

According to the findings presented in Fig. 9(a), when the jet velocity is below 1.0*U*, the pantograph experienced relatively constant reductions in aerodynamic drag regardless of its position in the air jet. The variations in the reduction rate were minimal, with a difference of less than 3%. This indicates that the location of the jet slot has a negligible effect on the aerodynamic drag of the pantograph. As the jet velocity increased, the aerodynamic drag reduction rate decreased as the distance between the jet slot and pantograph increased. Figure 14 shows the variations in the aerodynamic drag reduction rates of individual components with the distance between the jet slot and pantograph at jet velocities of 0.8*U* and 1.6*U*. For jet velocities below 1.0*U*, the position of the jet had minimal effect on the component of the pantograph. However, when the jet velocity surpassed 1.0*U*, the location of the jet had a notable impact on the base frame. Specifically, as the distance L_{jet} from the pantograph increased, the aerodynamic drag reduction rate in the base frame deceased.

Figure 15 shows the streamwise velocity distributions in a central vertical plane at different jet-slot positions and jet velocities of 0.8*U* and 1.6*U*. When the jet velocity was low, the streamwise flow remained dominant and the synthetic angle was small, as evidenced by the velocity distributions along the space lines in front of each component of the pantograph, as shown in Fig. 15(a) and Fig. 16(a). Irrespective of the position of the jet, its effects were limited to the base frame region and the under part of the bottom frame. However, as the jet velocity increased, the effect of the vertical jet flow became more pronounced, resulting in the amplification of the synthetic angle, rapid upward movement of air, and gradual expansion of the affected region encompassing the entire pantograph. When the jet slot is close to the pantograph, the air surrounding the base frame was drawn in by the jet and flowed in the reverse direction, leading to a negative pressure on the windward and a positive pressure on the leeward side of the base frame. However, as the jet position moved further away from the pantograph, the synthetic jet flow gradually lost its ability to effectively displace the air around the frame. Consequently, the air began to flow in the streamwise direction, leading to an increase in the windward pressure on the base frame. This transition from negative to positive pressure values increased the aerodynamic drag experienced by the base frame. The drag reduction rate decreased as the distance from the pantograph increased, as indicated in Fig. 14(b).

For the bottom frame of the pantograph, when the jet slot is close to the pantograph, the synthetic flow acted directly on the rods. Vortices were generated and shed from the leeward side of the rods, leading to a significant pressure difference. Therefore, the aerodynamic resistance was significantly higher than that in the scenario in which no air jets were present. As the jet slot progressively moved away from the pantograph, the synthetic flow gradually moved upward, causing the affected region to expand towards the upper sections. However, owing to the impact of the primary streamwise flow, the synthetic flow moved downward towards a location that was 0.2*H* away from the front edge of the pantograph, leading to a decrease in the velocity and aerodynamic drag of the bottom frame. Nonetheless, owing to the relatively small size of the rod structure, the resulting changes remained negligible.

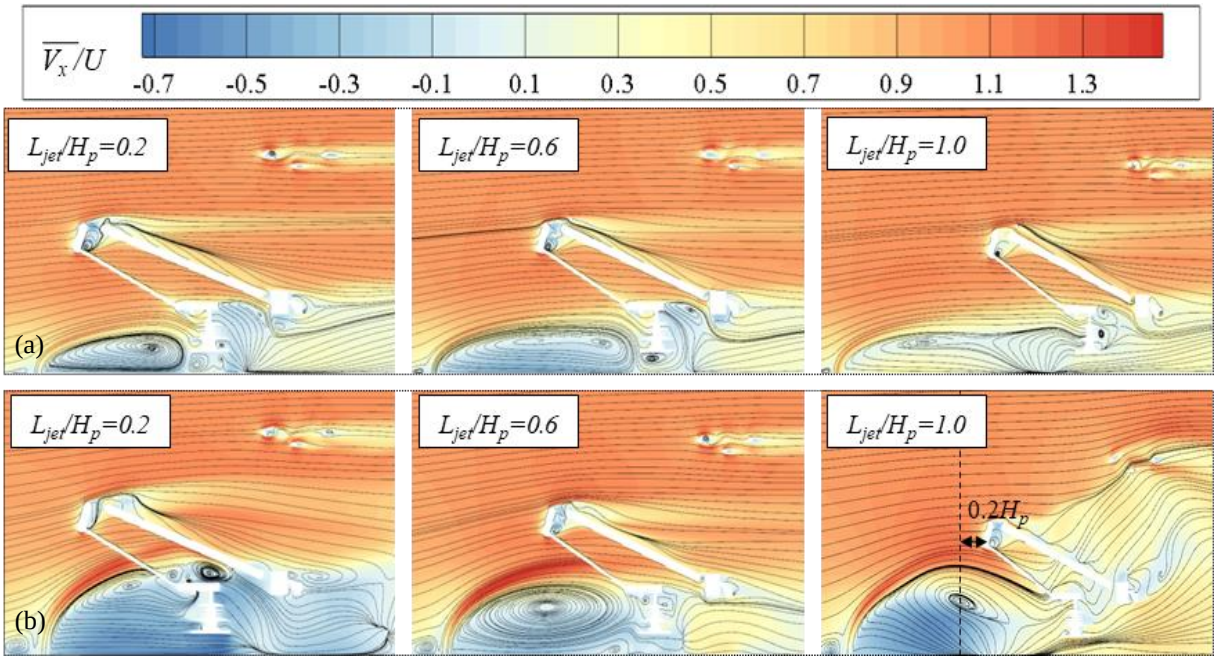

Fig. 15 Flow velocity change with jet locations in a vertical plane *Y=0* at different jet velocities: (a) V_{jet}/U = 0.8 and (b) V_{jet}/U = 1.6

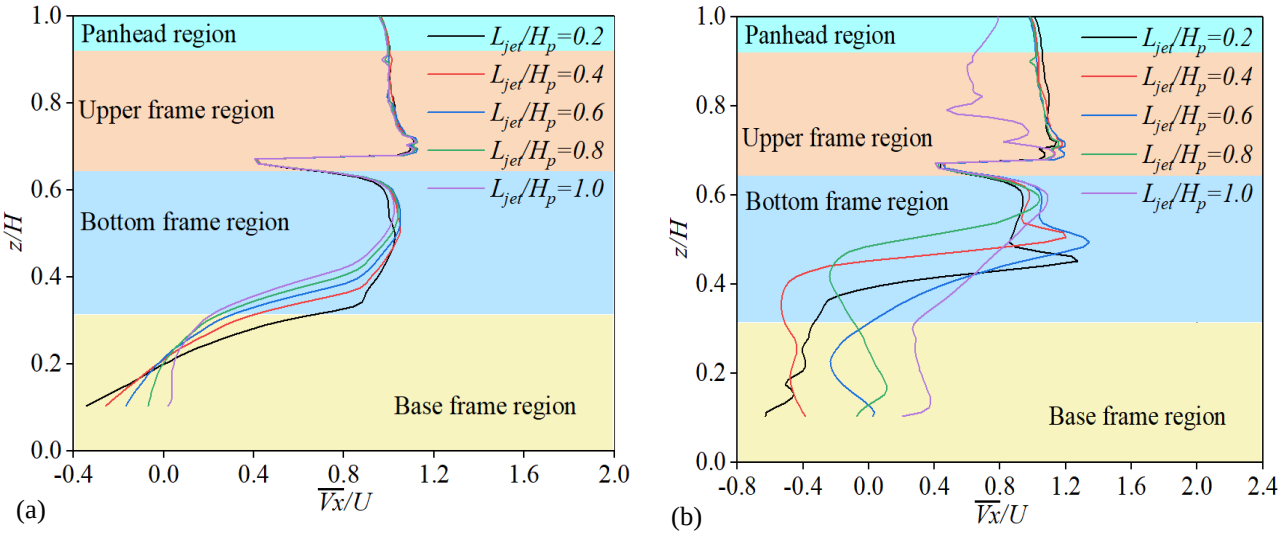

Fig. 16 $\overline{Vx}$ distributions along various spatial lines in front of the pantograph at different jet positions: (a) jet velocity V_{jet}/U = 0.8 and (b) jet velocity V_{jet}/U = 1.6

When the jet slot is close to the pantograph, the air velocity in front of the upper frame and panhead slightly changed owing to the dominant effect of the jet flow at the bottom. However, as the jet slot moved away from the pantograph, the synthetic flow moved downwards and crossed the pantograph rods with a decreasing velocity before rising upwards again under the influence of the main streamwise flow at the rear. This phenomenon decreased the streamwise component of the air velocity in the front region of the upper frame and panhead. However, as shown in Fig. 15(b) and 16(b), the upward flow field increased the velocity on the leeward side of the sliding strip. However, the impact of the jet positions on the upper frame and panhead was negligible compared with the flow change experienced by the base frame.

3.4 Effect of Jet-Slot Width on the Aerodynamics of Pantograph

Figure 17 shows the relationship between the aerodynamic drag reduction rate of the pantograph and the jet-slot width with a jet velocity of V_{jet}/U =1.0 and position of L_{jet}/H_p =0.2. It can be seen that the aerodynamic resistance of the base and upper frames decreased with the jet-slot width, while the aerodynamic drag of the panhead and bottom frame increased. The change in the aerodynamic drag with respect to the jet-slot width followed a pattern similar to that of the base frame.

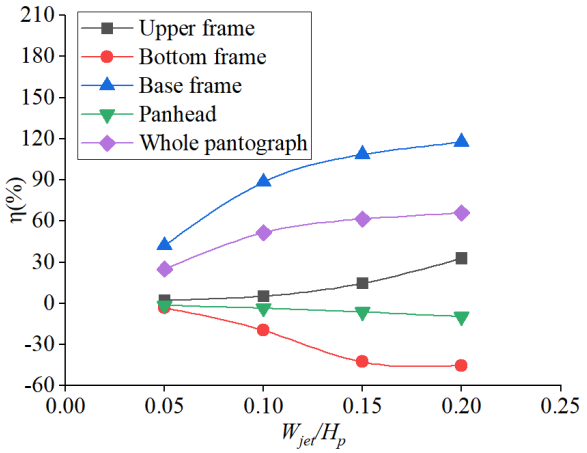

Fig. 17 Correlation between η and W_{jet} with a jet velocity of V_{jet}/U = 1.0 and position of L_{jet}/H_p = 0.2

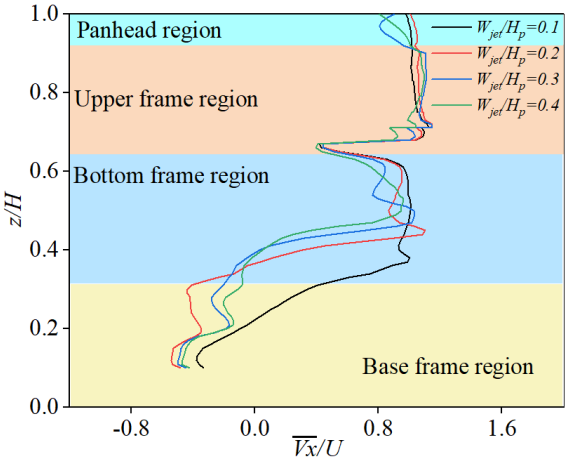

Fig. 19 $\overline{Vx}$ distributions along various spatial lines in front of the pantograph under different jet-slot widths at jet velocity of V_{jet}/U = 1.0 and position of L_{jet}/H_p = 0.2

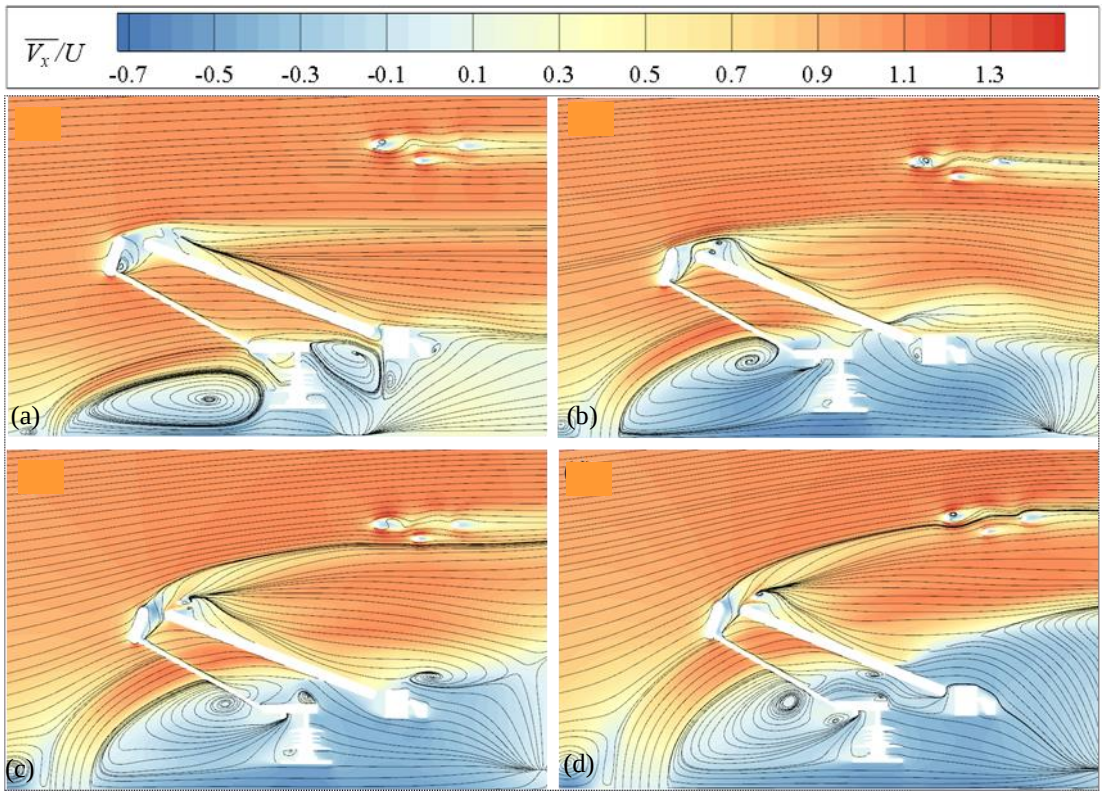

Fig. 18 Flow velocity in the middle vertical plane under different jet slot width with a jet velocity of V_{jet}/U = 1.0 at position L_{jet}/H_p = 0.2: (a) W_{jet}/H_p = 0.05; (b) W_{jet}/H_p = 0.1; (c) W_{jet}/H_p = 0.15; (d) W_{jet}/H_p = 0.2

As shown in Fig. 18, widening the jet-slot width gradually increased the energy of the jet, resulting in an increase in the synthetic flow angle. Furthermore, the impact area expanded from the base frame to the bottom frame, while the air in front of the base frame was fully absorbed by the upward synthetic flow. In accordance with Fig. 19, the streamwise flow velocity increased in the reverse direction, leading to an increase in the negative pressure exerted on the windward surface of the base frame. Consequently, the aerodynamic drag of the base frame decreased as the jet-slot width increased. However, for the bottom frame, although the flow velocity in front of the lower part decreased, the introduction of the synthetic flow directly acted on the upper part, which significantly enhanced the flow separation at the rear of the rods. Consequently, the negative pressure on the leeward surface of the bottom frame increased, which increased the aerodynamic drag of the bottom frame as the jet-slot width increased. Moreover, the enlarged synthetic flow angle induced the upward movement of the flow from the bottom frame to the upper frame, leading to a reduction in the streamwise

Table 1 Comparison of η under different mass flow with different jet velocities and jet slot widths

Q1		*Q2≈ 2Q1*	
parameter assignment	η_{Q1}/%	parameter assignment	η_{Q2}/%
V_{jet}/U=1.0 W_{jet}/H_p=0.05	25.03	*Scheme 1: Constant V_{jet} and variable W_{jet}* V_{jet}/U=1.0 W_{jet}/H_p=0.1	51.64
		Scheme 2: Variable V_{jet} and constant W_{jet} V_{jet}/U=2.0 W_{jet}/H_p=0.05	59.23

component of the velocity in front of it. Subsequently, the velocity in front of the top section of the upper frame increased owing to the incoming flow from the mainstream area, as shown in Fig. 19. Since the diameter of the lower section of the upper frame's rod was larger than that of the upper section, and the velocity increase at the top was smaller compared with the velocity decrease at the bottom, the upper frame experienced a reduction in aerodynamic drag as the jet-slot width increased. Finally, the flow velocity in front of the panhead decreased owing to the influence of the upward flow. However, the flow affected the rear carbon sliding plate instead of the front one, leading to an increase in the positive pressure on the front surface and an intensified negative pressure on the leeward side of the rear carbon sliding plate. Therefore, the panhead experienced an increase in aerodynamic resistance as the jet-slot width increased.

Based on the above investigation, it can be concluded that mass flow control is a significant factor in reducing the aerodynamic resistance of the pantograph. Increasing the jet velocity and widening the jet slot are both ways to increase the mass flow rate. To explore the contribution of the jet velocity and jet area under the same mass flow increment on the drag reduction of the pantograph, comparisons were made between different parameter assignments under the same mass flow rate, including the constant jet velocity and variable jet-slot width, and variable jet velocity and constant jet-slot width. As listed in Table 1, when multiplying the mass flow from *Q1* to *Q2*, the increase in η under scheme 2 (*variable V_{jet} and constant W_{jet}*) was greater than that of scheme 1 (*constant V_{jet} and variable W_{jet}*) with an approximate difference of 7.6%. In summary, under the same mass flow increment, increasing the jet velocity is more effective to reduce the aerodynamic drag of the pantograph than increasing the jet area.

3.5 Energy Efficiency Discussion

The above studies have proved the effectiveness of jet-flow control method in reducing the aerodynamic resistance of the pantograph. However, the active jet flow is an additional energy consumption source for the train, it is hard to evaluate the energy efficiency. In this section, dimensionless coefficient of the saved energy due to the train aerodynamic drag reduction C_{ES} and dimensionless coefficient of the consumed energy due to the jet flow C_{EC} were defined in Eq. (13) and (14), and the net energy saving can be calculated as $\triangle C_E$ in Eq. (15) (Che et al., 2023b).

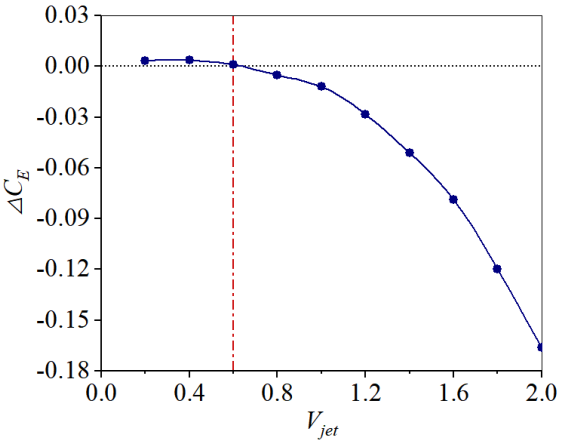

Fig. 20 Correlation between the net energy saving $\triangle C_E$ and jet velocity V_{jet}

$$C_{ES} = \frac{\Delta F_d U}{0.5\rho U^3 S} \tag{13}$$

$$C_{EC} = \frac{W_B}{0.5\rho U^3 S} = \frac{(0.5\rho V_{jet}{}^2 S_B)V_{jet}}{0.5\rho U^3 S} \tag{14}$$

$$\Delta C_E = C_{ES} - C_{EC} \tag{15}$$

where $\triangle F_d$ is the aerodynamic drag reduction value of the train with three cars; W_B represents the energy consumed by the jet flow and S_B is the area of the jet slot.

Since the optimal aerodynamic drag reduction was obtained when the jet slot positioned closer to the pantograph, the energy efficiency analysis was conducted under jet flow with L_{jet}/H_p=0.2 and W_{jet}/H_p=0.05. As indicated in Fig. 20, when the jet velocity exceeded 0.6 times the train speed, the net energy saving $\triangle C_E$ became negative and the absolute value increased rapidly with the increasing jet velocity. In this case, although higher jet velocity leads to greater aerodynamic drag reduction effect to the pantograph, the energy of the overall train with three coaches can only be saved at relative small jet velocities (V_{jet}/U＜0.6). The theoretical energy efficiency analysis was significant to provide guidance for the engineering application of the jet flow control technology in the future, thus comprehensive energy efficiency analysis should be taken into account in future studies.

4. CONCLUSION

A numerical approach was utilised to explore the effectiveness of the jet-flow control technique in reducing the pantograph's aerodynamic drag. The relationships between the aerodynamic drag of the pantograph and the position, velocity, and width of the jet slot were analysed. The results can be concluded as follows:

(1) The aerodynamic drag reduction rate of the pantograph did not differ significantly with the jet positions at jet velocities below 1.0U. However, as the jet velocity increased, the reduction rate decreased as the jet slot moved away from the pantograph. Thus, the jet slot should be positioned as close as possible to the pantograph.

(2) When the jet slot was located close to the pantograph (L_{jet}/H < 0.6), the aerodynamic drag reduction rate continuously increased with the jet velocity. The enhanced drag reduction effect with increasing speed weakened as the jet slot moved away from the pantograph, and remained relatively stable once the jet velocity surpassed 1.2U.

(3) Increasing the jet-slot width also greatly enhanced the drag reduction effect of the pantograph. In other word, the mass flow control of the jet is a primary factor affecting the aerodynamics of the pantograph. However, at the same increasing mass flow, an increase in the jet velocity contributed more towards reducing the aerodynamic resistance than an increase in the jet area.

(4) The energy of the whole train can be saved when the jet velocity was blow 0.6U, and the net energy saving changed to negative with its absolute value increased with the increasing jet velocity.

Findings in this study provide significant engineering guidance for the prospective implementation of air-jet techniques in the low-resistance design of high-speed trains. However, this paper still has some limitations. For engineering applications, the effects of jet parameters on the whole train aerodynamics, including the aerodynamic noise, will be comprehensively studied in the future. In addition, further comprehensive energy efficiency analysis on other variable parameters should be taken into account.

ACKNOWLEDGEMENTS

The study in this paper was supported by the National Natural Science Foundation of China (52002290) and the National Science Foundation of Guangdong Province (2022A1515010011). The Big Data Center for Biomedical Research of Wuyi University was acknowledged for providing computational resources.

CONFLICT OF INTEREST

The author(s) have no conflicts to disclose.

AUTHORS CONTRIBUTION

S. Huang: Conceptualization, Writing-Original draft. **B. D Zhang:** Investigation, Validation. **Z. W. Li:** Methodology, Supervision, Writing- review & editing. **J. P. Zhao:** Data curation, Visualization. **W. J. Peng:** Investigation. **J. R. Lin:** Visualization.

REFERENCES

Ansys, Inc. (2019). *Ansys Fluent User's Guide*. (2019R2).

Che, Z. X., Huang, S., Li, Z. W., & Chen, Z. W. (2023a). Aerodynamic drag reduction of high-speed maglev train based on air blowing/suction. *Journal of Wind Engineering and Industrial Aerodynamics*, *233*, 105321. https://doi.org/10.1016/j.jweia.2023.105321

Che, Z. X., Chen, Z. W., Ni, Y. Q., Huang, S., & Li, Z. W. (2023b). Research on the impact of air-blowing on aerodynamic drag reduction and wake characteristics of a high-speed maglev train. *Physics of Fluid*, *35*, 115138. https://doi.org/10.1063/5.0175323

Chen, Y., Gao, Y., Wang, Y. G., Yang, Z. G., & Li, C. L. (2018). Wind tunnel experimental research on the effect of guide cover on aerodynamic noise of pantograph. *Technical Acoustics*, *37*(5), 475-481. https://doi.org/10.16300/j.cnki.1000-3630.2018.05.012

Dong, T. Y., Liang, X. F., Krajnović, S., Xiong, X. H., & Zhou, W. (2019). Effects of simplifying train bogies on surrounding flow and aerodynamic forces. *Journal of Wind Engineering & Industrial Aerodynamics*, *191*, 170-182. https://doi.org/10.1016/j.jweia.2019.06.006

Huang, K. L., Yuan, T. C., Yang, J., Miao, X. D., & Song, R. G. (2020). Approach of reduction of aerodynamic noise of pantograph cavity of high-speed train based on jet. *Journal of the China Railway Society*, *42* (7), 50-56. https://doi.org/10.3969/j.issn.1001-8360.2020.07.006

Huang, S., Hemida, H., & Yang, M. Z. (2016). Numerical calculation of the slipstream generated by a CRH2 high-speed train. *Proceedings of the Institution of Mechanical Engineering, Part F: Journal of Rail and Rapid Transit*, *230*(1), 103-116. https://doi.org/10.1177/0954409714528891

Huang, S., Yu, Y., Li, Z. W., & Che, Z. X. (2021). Study of aerodynamic drag reduction of high-speed train based on tail jet-flow control. *Journal of the China Railway Society*, *43*(11), 38-46. https://doi.org/10.3969/j.issn.1001-8360.2021.11.005

Ito, M. (2000). Improvement to the aerodynamic characteristics of Shinkansen rolling stock. *Proceedings of the Institution of Mechanical Engineers, Part F: Journal of Rail and Rapid*

Transit, *214*(3), 135-143. https://doi.org/10.1243/0954409001531261

Kim, H., Hu, Z. W., & Thompson, D. (2020). Numerical investigation of the effect of cavity flow on high-speed train pantograph aerodynamic noise. *Journal of Wind Engineering and Industrial Aerodynamics*, *214*, 104159. https://doi.org/10.1016/j.jweia.2020.104159

Lee, Y., Rho, J., Kim, K. H., Lee, D. H., & Kwon, H. B. (2015). Experimental studies on the aerodynamic characteristics of a pantograph suitable for a high-speed train. *Proceedings of the Institution of Mechanical Engineering, Part F: Journal of Rail and Rapid Transit*, *229*, 136-149. https://doi.org/10.1177/0954409713507561

Li, T., Qin, D., Zhou, N., Zhang, J. Y., Zhang, W. H. (2022). Numerical study on the aerodynamic acoustic scale effects for high-speed train body and pantograph. *Applied Acoustics*, *196*, 108886. https://doi.org/10.1016/j.apacoust.2022.108886

Li, X. F., Zhou, D., Jia, L. R., & Yang, M. Z. (2018). Effects of yaw angle on the unsteady aerodynamic performance of the pantograph of a high-speed train under crosswind, *Journal of Wind and Industrial Aerodynamics*, *182*, 49-60. https://doi.org/10.1016/j.jweia.2018.09.009

Li, X. F., Zhou, D., Jia, L. R., & Yang M. Z. (2023). Numerical study of the influence of dome shape on the unsteady aerodynamic performance of a high-speed train's pantograph subjected to crosswind. *Journal of Traffic and Transportation Engineering*, *10*(1), 13-30. https://doi.org/10.1016/j.jtte.2021.08.005

Liu, X., Deng, J., Zheng, Y., & Pan, G. F. (2013). Impact of aerodynamics of pantograph of a high-speed train on pantograph-catenary current collection. *Journal of Zhejiang University (Engineering Science)*, *47*(3), 558-564. https://doi.org/10.3785/j.issn.1008-973X.2013.03.024.

Liu, H. T., & Xu, Z. L. (2018). Study on drag and noise reduction of pantograph rods based on bionic non-smooth structures. *Noise and Vibration Control*, *38* (Z1), 269-272. https://doi.org/10.3969/j.issn.1006-1355.2018.Z1.056

Meng, S., Meng, S., Wu, F., Li, X. L., & Zhou, D. (2021). Comparative analysis of the slipstream of different nose length on two trains passing each other. *Journal of Wind Engineering & Industrial Aerodynamics*, *208*, 104457. https://doi.org/10.1016/j.jweia.2020.104457

Mitsumoji, T., Sueki, T., Yamazaki, N., Sato, Y., Ikeda, M., Takinami, R., Gejima, H., & Fukagata K. (2015). Aerodynamic noise reduction of a pantograph panhead by applying a flow control method. *Noise and Vibration Mitigation for Rail Transportation Systems, Notes on Numerical Fluid Mechanics and Multidisciplinary Design*, *126*, 515-522. https://doi.org/10.1007/978-3-662-44832-8_60

Niu, J. Q., Liang, X. F., & Zhou, D. (2017). Aerodynamic impact of pantograph located on the high-speed train passing through a station. *Journal of Vibration Engineering 2017; 30*(2), 333-340. https://doi.org/10.16385/j.cnki.issn.1004-4523.2017.02.021

Niu, J. Q., Wang, Y. M., Zhang, L., & Yuan, Y. P. (2018). Numerical analysis of aerodynamic characteristics of high-speed train with different train noise length. *International Journal of Heat and Mass Transfer*, *127*, 188-199. https://doi.org/10.1016/j.ijheatmasstransfer.2018.08.041

Niu, J. Q., Wang, Y. M., Liu, F. & Chen, Z. W. (2020). Comparative study on the effect of aerodynamic braking plates mounted at the inter-carriage region of a high-speed train with pantograph and air-conditioning unit for enhanced braking. *Journal of Wind Engineering & Industrial Aerodynamics*, *206*, 104360. https://doi.org/10.1016/j.jweia.2020.104360

Satio, M., Mizushima, F., Wakabayashi, Y., Kurita, T., Nakajima, S., & Hirasawa, T. (2021). Development of new low-noise pantograph for high-speed trains. *Noise and Vibration Mitigation for Rail Transportation Systems, Notes on Numerical Fluid Mechanics and Multidisciplinary Design*, *150*, 81-89. https://doi.org/10.1007/978-3-030-70289-2

Shur, M. L., Spalart, P. R., Strelets, M. Kh., & Travin, A. K. (2008). A hybrid RANS-LES approach with delayed-DES and wall-modelled LES capabilities. *International Journal of Heat and Fluid Flow*, *29*, 1638-1649. https://doi.org/10.1016/j.ijheatfluidflow.2008.07.001

Sun, Z. K., Wang, T. T., & Wu, F. (2020). Numerical investigation of influence of pantograph parameters and train length on aerodynamic drag of high-speed train. *Journal of Central South University*, *27*, 1334-1350. https://doi.org/10.1007/s11771-020-4370-6

Tan, C. D., Zhou, D., Chen, G., Sheridan, J., & Krajnović, S. (2020). Influence of marshalling length on the flow structure of a maglev train. *International Journal of Heat and Fluid Flow*, *85*, 108604. https://doi.org/10.1016/j.ijheatfluidflow.2020.108604

Tan, X. M., Yang, Z. G., Tan, X. M., Wu, X. L., & Zhang, J. (2018). Vortex structure and aeroacoustic performance of the flow field of the pantograph. *Journal of Sound and Vibration*, *432*, 17-32. https://doi.org/10.1016/j.jsv.2018.06.025

Tang, X., Zhou D. W., & Liang, X. F. (2015). Aerodynamic load on pantograph of high-speed train passing into and out tunnels. *Journal of Central South University (Science and Technology)*, *46*(5), 1923-1928. https://doi.org/10.11817/j.issn.1672-207.2015.05.047

Wang, J. B., Minelli, G., Dong, T. Y., Chen G., & Krajnović, S. (2019). The effect of bogie faring on the slipstream and wake flow of a high-speed train. An IDDES study. *Journal of Wind Engineering & Industrial Aerodynamics*, *191*, 183-202. https://doi.org/10.1016/j.jweia.2019.06.010

Wang, J. B., Minelli, G., Zhang, Y., Zhang, J., Krajnović, S. & Gao, G. J. (2020). An improved delayed detached eddy simulation study of the bogie cavity length effects on the aerodynamic performance of a high-speed train. *Proceedings of the Institution of Mechanical Engineers, Part C: Journal of Mechanical Engineering Science*, *234*(12), 2386-2401. https://doi.org/10.1177/09544062209076

Wang, Y. C., Yu, Y. Z., Gai, J., & Jiang, H. Y. (2022). Simulation analysis of aerodynamic characteristics of streamlined pantograph for high speed train. *Journal of Dalian Jiaotong University*, *43* (1), 7-42. https://doi.org/10.13291/j.cnki.djdxac.2022.01.007

Xia, C., Wang, H. F., Shan, X. Z., Yang, Z. G., & Li, Q. L. (2017). Effects of ground configurations on the slipstream and near wake of a high-speed train. *Journal of Wind Engineering & Industrial Aerodynamics*, *168*, 177-189. https://doi.org/10.1016/j.jweia.2017.06.005

Xiao, C. H., Yang, M. Z., Tan, C. D., & Lu, Z. J. (2020). Effects of platform sinking height on the unsteady aerodynamic performance of high-speed train pantograph. *Journal of Wind Engineering and Industrial Aerodynamics*, *204*, 104284. https://doi.org/10.1016/j.jweia.2020.104284

Xiu, Y. L., & Du, L. M. (2016). Influence of aerodynamic force on pantograph deformation during high speed train running in tunnel. *Journal of Dalian Jiaotong University*, *37*(4), 50-54. https://doi.org/10.1329/j.cnki.djdxac.2016.04.013

Xu, Z. L., Liu, H. T., Wang, C. W., & Chen, Y. H. (2020). Study on drag and noise reduction of pantograph rods in high speed train. *Journal of East China Jiaotong University*, *37*(2), 1-6. https://doi.org/10.16749/j.cnki.jecjtu.2020.02.001

Yan, Y. Z., Xu, X. H., Wang, X. Z., Geng, H. S., & Huang, S. J. (2022). Simulation of optimization study on aerodynamic drag reduction of high-speed train pantograph, *Mechanics in Engineering*, *44*(5), 276-284. https://doi.org/10.6052/1000-0879-21-372

Yao, Y., Sun, Z., Li, G., Prapamonthon, P., Cheng, G., & Yang, G. (2022). Numerical investigation on aerodynamic drag and noise of pantographs with modified structures. *Journal of Applied Fluid Mechanics*, *15*(2), 617-631. https://doi.org/10.47176/jafm.15.02.32849

Yao, Y. F., Sun, Z. X., Liu, W., & Yang, G. W. (2020). Analysis of aerodynamic noise characteristics of pantograph in high-speed train. *Acta Scientiarum Naturalium Universitatis Pekinensis*, *56*(3), 385-398. https://doi.org/10.13209/j.0479-8023.2020.014

Zhang, C. L., Liu, H. T., Zhou, X., Yang, C. H., & Xiao, Q. (2021). Reduction of drag and noise for pantograph rods with spanwise waviness structure. *Noise and Vibration Control*, *41*(6), 126-133. https://doi.org/10.3969/j.issn.1006-1355.2021.06.021

Zhang, L., Yang, M. Z. & Liang, X. F. (2018). Experimental study on the effect of wind angle on pressure distribution of train streamlined zone and train aerodynamic forces, *Journal of Wind Engineering and Industrial Aerodynamics*, *174*, 330-343. https://doi.org/10.1016/j.jweia.2018.01.024

Zhang, L., Zhang, J. Y., Li, T., & Zhang W. H. (2017). Research on unsteady aerodynamic characteristics of pantographs in different positions of high-speed trains. *Journal of Mechanical Engineering*, *53*(12), 147-155. https://doi.org/10.3901/JME.2017.12.147